

Custom Made Optical Pulses for Photon Echo Spectroscopy

Maaïke T. W. Milder

August 10, 2005

September 2004 - July 2005

Ultrafast Laser and Spectroscopy Group

Supervisor: M.S. Pshenichnikov



Abstract

Nonlinear optical techniques are widely used to study energy transport in nanoscale objects. In particular photon echo spectroscopy can be used to determine if the energy transport is coherent or not. In this project a novel phase sensitive nonlinear technique is proposed. The main feature of this technique is the application of two phase-locked pulses. The relative phase and the delay between the two pulses is set electronically by a pulse shaper based on a spatial light modulator (SLM). The use of an SLM ensures phase stability. The proposed method is tested on a model system of solutions of the dye molecule DTTCI in ethylene glycol and acetonitrile. The obtained results demonstrated that the parameters from the experimental data agree with those from previous studies. Hence, the proposed technique can be further developed for energy transport studies.

Contents

| | | |
|----------|--|-----------|
| 1 | Introduction | 5 |
| 1.1 | Solute-solvent interactions | 5 |
| 1.2 | Spectroscopy | 6 |
| 1.3 | Nonlinear spectroscopy | 6 |
| 1.4 | Energy transport in nanowires | 7 |
| 1.5 | Outline | 7 |
| 2 | Photon Echo Spectroscopy | 8 |
| 2.1 | Theoretical background | 9 |
| 2.2 | Design of the experiments | 11 |
| 3 | Titanium Sapphire Laser | 13 |
| 3.1 | Pulse generation | 13 |
| 3.2 | Kerr-lens mode-locking | 13 |
| 3.3 | Stability zones | 13 |
| 3.4 | Setup | 14 |
| 3.5 | Results | 15 |
| 4 | Spatial Light Modulator (SLM) | 17 |
| 4.1 | Pulse Shaping | 17 |
| 4.2 | Liquid crystal spatial light modulator (SLM) | 19 |
| 4.3 | Set-up: shaper and detection geometry | 19 |
| 4.4 | Alignment and calibration | 20 |
| 4.5 | Creation of a pulse pair | 21 |
| 4.6 | Results | 23 |
| 5 | Acquirement of the Correlation Function | 24 |
| 5.1 | Initial settings | 24 |
| 5.2 | Experiments | 25 |
| 5.3 | Results | 26 |
| 6 | Conclusion | 28 |
| 7 | Appendix | 30 |

Chapter 1

Introduction

1.1 Solute-solvent interactions

In liquids, the processes that follow after photoexcitation heavily depend on the solvent dynamics. The solute-solvent interactions in liquids can change the shape and the position of the potential energy surfaces of the system (Fig.1.1). One of the important aspects resulting from the interaction between solute and solvent is the (de-)stabilization of the excited state, thereby changing the excitation energy gap. To get a complete picture of dynamical molecular processes in the liquid state the solvation process should be examined.

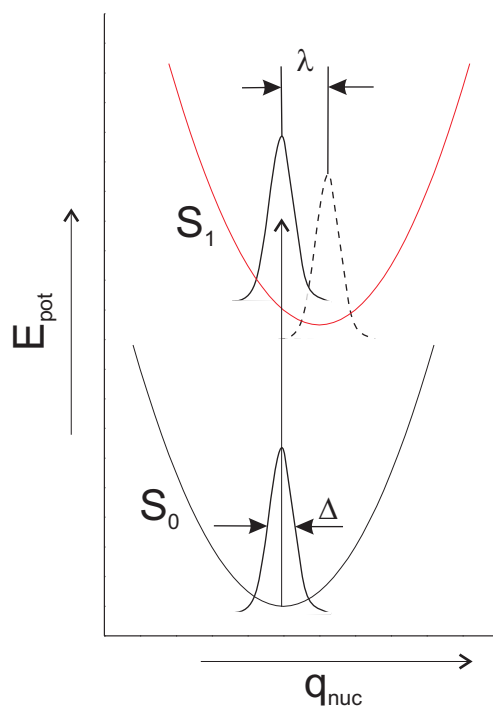


Figure 1.1: Schematic picture of the harmonic potential energy surfaces resulting from solute-solvent interactions. The ground and excited state wavefunctions are depicted by solid lines, the relaxed excited states is depicted by a dashed line. The coordinate on the x-axis has a collective nature and can be referred to as a generalized solvent coordinate. The parameters Δ and λ represent the linewidth and the Stokes shift respectively.

The energy diagram in figure 1.1 can serve as a simple guideline to investigate solvation dynamics. Interaction with solvent molecules allows the electronically excited system to relax to the lowest vibrational mode. The absorption and emission bands in liquids are broad and often featureless, due to the averaging of the local environments of solute molecules. Linear optical experiments can not be used to discriminate between different dynamical processes. Therefore, non-linear optical spectroscopy will be used to study the relaxation pathways in solutions [1].

The effects of solvation are visible in the fluctuations of energy levels (frequency fluctuations) in the solute. With optical spectroscopy the energy difference $\Delta E(t)$ between levels can be probed, hence the solvation effects will appear as fluctuations in these differences $\delta\Delta E(t)$. The energy fluctuations can be described using a correlation function Eq.1.1.

$$C_{\Delta E(t)} = \frac{\langle \delta\nu(0)\delta\nu(t) \rangle}{\langle \delta\nu^2 \rangle} \quad (1.1)$$

Photon echo spectroscopy can be used to study the energy fluctuations described by the correlation function.

1.2 Spectroscopy

Irradiation of a sample with light, results in the transfer of molecules from the ground state to an excited state. When the system relaxes back to the ground state the sample will emit photons. The time between irradiation and emission is the lifetime of the excited state. Observation of the characteristics of the emitted photons with a detector reveals system properties. Two different types of spectroscopy can be distinguished. Basic absorption and emission spectroscopy are examples a type of spectroscopy that operates in the frequency domain. A second type of spectroscopy, such as pump-probe, and photon echo, operates in the time domain and is referred to as nonlinear spectroscopy (fig.1.2). Here, the excitation light pulses are short (subpicosecond), so they are on the same time scale as the system dynamics. As a consequence, the width of these pulses exceeds the linewidth of the optical transition by far and the frequency sensitivity is substantially lowered. To examine the solvation dynamics in time, a specific type of photon echo spectroscopy will be used.

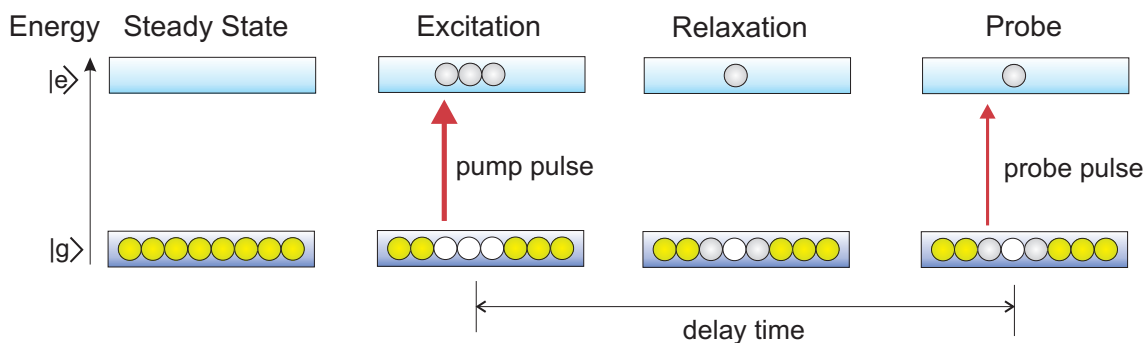


Figure 1.2: Schematic view of pump-probe experiments. The pump pulse causes photoexcitation and the population in the ground state (green balls) is partially transferred to the excited state (grey balls) leaving behind ‘holes’ in the ground state (white balls). The probe pulse detects the population decay from the excited state to the ground state.

1.3 Nonlinear spectroscopy

Interaction of a sample with light induces a time-dependent polarization $P(r, t)$ that generates a signal field $E_s(r, t)$. The first nonlinear polarization in liquids is $P^{(3)}(r, t)$, because $P^{(2)}(r, t)$ is zero due to symmetry restrictions. Perturbation theory is used together with the density matrix formalism to describe the nonlinear polarization in a multi-particle system. Time-evolution of the density matrix elements is governed by the Liouville equation. Perturbative treatment of these equations leads to the frequency correlation function (Eq.1.1). A full description of this formalism can be found in references [1], [2] and [3]. The theoretical section in this report will be based on these descriptions.

The multimode Brownian oscillator model (MBO) is used to describe the two-level system. In this model both the ground and the excited state potentials are approximated to be harmonic. The bath modes of the corresponding solvent molecules are set as a series of harmonic oscillators, which are coupled to the harmonic nuclear potentials (q_{nuc}).

1.4 Energy transport in nanowires

Controlling of energy transport in molecular aggregates is the subject of many recent studies [4],[5],[6]. The most interesting regime of transport is the coherent one, which is more efficient than diffusive motion. In coherent transport the phase of the system will be preserved. Photon echo spectroscopy is a nonlinear technique that is sensitive to the phase of a system and can therefore determine if there is coherent transport in a system. The technique developed in this project to control the phase between pulses in a heterodyne detected pump-probe experiments can be adapted to 2D photon echo experiments. These experiments will be used to study coherent energy transport in supramolecular arrays of highly organized chromophores.

1.5 Outline

A specific type of photon echo spectroscopy will be used to obtain information about solvation dynamics. In chapter 2 the theory behind photon echo spectroscopy will be addressed. The simplest way to obtain the correlation function from nonlinear optical experiments is determined and this is by making use of heterodyne detected pump-probe (HDPP) spectroscopy. The design of the HDPP experiments will result from restrictions and requirements described in this chapter.

A home-built femtosecond Ti:sapphire laser will be used to generate ultrashort pulses. Generation of 10 fs pulses with a variable repetition rate and high energies makes this laser a suitable tool in heterodyne detected pump-probe spectroscopy. The principles and set-up of this laser will be discussed in chapter 3.

To apply to the strict requirements in heterodyne detected pump-probe spectroscopy regarding time and phase control between consecutive pulses, a spatial light modulator (SLM) will be used. This device has proven its value in generating specific waveforms in an entirely electronic way. The properties and incorporation of the SLM in the set-up will be described in chapter 4.

The experimental details of the heterodyne detected pump-probe measurements on solutions of DTTCI are presented in chapter 5. This chapter also discusses the data that are obtained from the experiments.

Finally, this report will be concluded in chapter 6. The possibility of performing heterodyne detected pump-probe spectroscopy with the use of a spatial light modulator and its ability to obtain the solute-solvent correlation function will be discussed.

Chapter 2

Photon Echo Spectroscopy

Photon echo spectroscopy requires a specific pulse sequence (Fig.2.1). The first two pulses excite the system and the third (probe) pulse generates a third order polarization $P^{(3)}$. The fourth pulse is used to heterodyne the signal field induced by $P^{(3)}$. The signal field E_s of the emitted light is created by three incoming fields. The wavevector of the signal field has a direction that is shared with the probe field (E_3 or E_4), in the specific geometry that will be used in the experiments (Fig.2.2). In this situation the phase matching condition is $\vec{k}_s = -\vec{k}_1 + \vec{k}_2 + \vec{k}_3$, where the direction of the wavevectors k_1 and k_2 is equal.

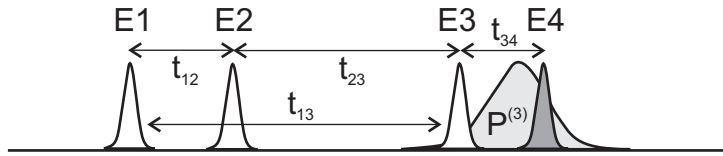


Figure 2.1: Three-pulse photon echo pulse sequences. Relevant times t_{12} , t_{23} , t_{13} and the heterodyne pulse time t_{34} are indicated.

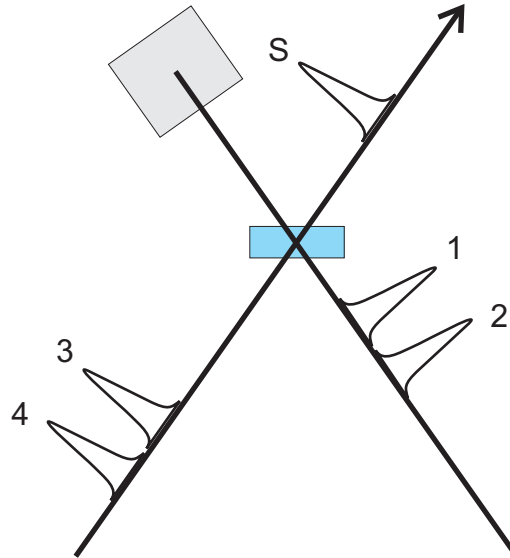


Figure 2.2: Phase matching conditions for three-pulse photon echo experiments. The signal field is detected along the direction of the probe pulses.

Interactions of the system with the pulses can be described by Feynman diagrams as in appendix 1. The diagrams show that there are two different field sequences that are resonant with the two-level system. The sequences $E_1^*E_2E_3$ and $E_1E_2^*E_3$ both are resonant, however in the derivation of all different terms in the final signal E_s only $E_1^*E_2E_3$ will be considered Eq.2.1. The derivation using $E_1E_2^*E_3$ will not add any new information and is therefore omitted. A combination of the

two excitation fields $E_1^*E_2$ with either the third or fourth field ($E_1^*E_2E_3$, and $E_1^*E_2E_4$) generates the signal field E_s . The observable intensity is the interference of E_s with either E_3 or E_4 and leads to the expression in Eq.2.1.

$$I_{tot} \propto |E_s + E_3 + E_4|^2 = |E_1^*E_2E_3|^2 + |E_1^*E_2E_4|^2 + 2\left(|E_3|^2 + |E_4|^2\right) + 4Re(E_3E_4^*) + 2Re(E_1^*E_2E_3E_3^*) + 2Re(E_1^*E_2E_3E_4^*) + 2Re(E_1^*E_2E_4E_4^*) \quad (2.1)$$

The first two terms in Eq.2.1 are homodyne contributions, which can be neglected because they are small. The third and fourth term correspond to the intensities of the third and fourth pulse and will give a constant background that is subtracted by using a lock-in detector. The fifth term is the interference term between the third and fourth pulse and will also result in a small value that is neglected. The last three terms together form the total observable signal, S^{tot} . The term of interest in this sum exclusively is the echo signal $E_1^*E_2E_3E_4^*$, the other two terms (pump-probe contributions) cannot be separated from the echo signal in a direct way.

2.1 Theoretical background

Solutes can often be approached as a two level system with a ground state and an electronically excited state. With the first and second pulse, the system is brought to a higher energy level. These pulses have a bandwidth of approximately 100 nm, and excite a vibrational manifold. A wavepacket is formed that can be described as if it were traveling between the walls of the harmonic potential of the excited state until it has decayed to the lowest vibrational state. These oscillations can be observed in photon echo experiments. Reaction of the solvent molecules to the new position of the nuclei of the solute in the excited state and vice versa give rise to the second type of oscillations. The local vibrations taking place at different solute molecules average out and lead to a signal that can be approximated as an exponential decay. This decay is also observed by photon echo spectroscopy.

All optical experiments that fall under the generic term of four-wave mixing (three incoming and one outgoing photon), can be described with one common formalism [2]. The basic theoretical model of a two-level system is described with Feynman diagrams (appendix 1), however this description assumes homogeneous broadening of the transition energy. The homogenous broadening implies random fluctuations in the transition frequency of the oscillators, without any form of memory of the previous value. However, these fluctuations in the oscillator are not completely random in solute-solvent systems. The correlation function $M(t)$ describes intramolecular interactions and the intermolecular solute-solvent coupling dynamics (Eq.2.2). The function $M(t)$ can be related to the correlation function $C(t)$ (chapter 1) in the so-called linear response approximation [2]. In this approximation the ground state dynamics are indistinguishable from the excited state dynamics.

$$M(t) = \frac{\langle \Delta\omega(t)\Delta\omega(0) \rangle}{\langle \Delta\omega^2 \rangle} \quad (2.2)$$

The changes in the transition frequency in solvent relaxation dynamics can be simulated reasonably well using the multimode Brownian oscillator model (MBO). This model takes inhomogeneous transition broadening into account. An extensive description of this model leading to the final optically observable signal can be found in references [2] and [7]. Key elements in the MBO theory is the correlation function $M(t)$, that mimics the correlation in the transition frequency shifts. With the use of photon echo spectroscopy these functions can be obtained. Once these functions are known, all linear and nonlinear optical properties of a system can be calculated. In the simulations that are used, the MBO model is restricted to two cases, the weakly damped mode and the overdamped mode.

The condition for a weakly damped mode is $\gamma_j \ll \omega_j$ and the system-bath correlation function reduces to Eq.2.3.

$$M(t) = \exp\left(\frac{-\gamma_j t}{2}\right) \left[\cos(\omega_j t) + \frac{\gamma_j}{2\omega_j} \sin(\omega_j t) \right] \quad (2.3)$$

Here $1/\gamma$ represents the population life time of the j -th level. For this situation the coupling strength parameters λ and Δ are given by Eq.2.4.

$$\lambda = \frac{\Delta^2}{\omega} \tanh\left(\frac{\hbar\omega_j}{2k_bT}\right) \quad (2.4)$$

In the case of an overdamped mode, which is used to represent solvation effects that cause the exponential decay observed in pump-probe data, the condition is $\gamma_j \gg \omega_j$. The correlation function M is represented by Eq.2.5.

$$M(t) = \exp(-\Lambda t) \quad (2.5)$$

A physical meaning can be connected to Λ , it is the inverse correlation time of the system-bath fluctuations (Eq.2.6).

$$\Lambda = \frac{\omega^2}{\gamma_j} \quad (2.6)$$

In this case the coupling strength parameter λ is given by Eq. 2.7.

$$\lambda = \frac{\Delta^2 \hbar}{2k_bT} \quad (2.7)$$

As is formally derived from the MBO model, the photon echo signal S yields four nonlinear response functions, resulting from the four resonant Feynman diagrams for this situation (appendix 1). The assumption that the correlation function is static and does not deviate much from $M(t)=1$ on the time scale t_{34} enables the use of a Taylor expansion around t_{23} . Applying these restrictions finally results in an expression for S (Eq.2.8 to Eq.2.10). The signal S is equal to the echo term in the total intensity given in Eq.2.1. The total correlation function M^{tot} is composed of two contributions from the overdamped and the weakly damped situation. From Eq.2.3 and Eq.2.5 it is observed that M approaches the value of 1 at long time delays. To ensure that this is also the case in M^{tot} , a normalization factor is added.

$$\begin{aligned} S^{(3)}(t_{34}, t_{23}, t_{12}) \propto & \exp(-1/2\Delta^2 t_{12}^2 - 1/2\Delta^2 t_{34}^2 + 1/2\Delta^2 t_{12} t_{34} M(t_{23})) \times \\ & \cos(\lambda t_{34}(1 - M(t_{23})) \times \cos(\lambda t_{34}(1 - M(t_{23}) - \phi_{12} + \phi_{34})) + \\ & \exp(-1/2\Delta^2 t_{12}^2 - 1/2\Delta^2 t_{34}^2 - 1/2\Delta^2 t_{12} t_{34} M(t_{23})) \times \\ & \cos(\lambda t_{34}(1 - M(t_{23})) \times \cos(\lambda t_{34}(1 - M(t_{23}) + \phi_{12} + \phi_{34})) \end{aligned} \quad (2.8)$$

$$M^{tot} = aM_{overdamped} + (1 - a)M_{weakly damped} \quad (2.9)$$

$$\lambda^{tot} = \lambda_{overdamped} + \lambda_{weakly damped} \quad (2.10)$$

The signal is observed by using the specific pulse sequence in photon echo spectroscopy. In normal experiments (echo peak shift, time gated photon echo), only the exponential terms in Eq.2.8 are detected, while the techniques are not sensitive to the oscillatory part. Upon integration over t_{34} the oscillatory term is lost. The result is that of the two parameters that determine the frequency broadening only Δ is observed. The fluctuation dissipation theorem relates the value obtained for Δ to λ by Eq. 2.4. This only gives an indication for the upper limit of the coupling parameter λ and does not result in the real value of λ . The parameters λ and Δ in calculations of the linear spectroscopic properties represent the Stokes shift (shift between absorption and relaxed emission spectra) and the width of the absorption spectrum respectively.

2.2 Design of the experiments

The simplest method to obtain the real value of λ and not just the upper limit dictated by the value of Δ in the high-temperature limit (Eq. 2.7), can be deduced from Eq.2.8. The requirements to perform experiments that observe λ directly is control over the time differences, t_{34} and t_{23} and the phase setting, ϕ_{34} . This can be achieved by setting $t_{12} = 0$ in classical photon echo experiments turning them into heterodyne detected pump-probe (HDPP) experiments. A three-pulse instead of a classical four pulse sequence is used and the signal will then reduce to Eq.2.11. This signal of interest S , made up from the interaction $E_1^*E_2E_3E_4^*$ in Eq.2.1 is no longer referred to as the echo signal, but it will be called the HDPP signal in the remainder of the report.

$$S^{(3)}(t_{34}, t_{13}) = \exp(-1/2\Delta^2 t_{34}) \left[\cos(2\lambda t_{34}(1 - M(t_{13})) + \phi_{34}) + \cos(\phi_{34}) \right] \quad (2.11)$$

The experiments carried out are therefore heterodyne detected pump-probe (HDPP) measurements (Fig.2.3).

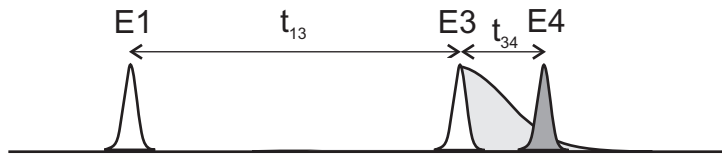


Figure 2.3: Heterodyne pump-probe (special type of photon echo) pulse sequences $t_{12} = 0$, hence pulse 1 and 2 overlap. Relevant time t_{13} and the heterodyne pulse time t_{34} are indicated.

The exponential term in Eq.2.11 damps the signal when t_{34} is increased. The second term in the equation is an oscillatory part that increases with t_{34} and that holds the correlation function.

By controlling the time and the phase between the third, probe pulse and the fourth, heterodyne pulse, the HDPP signal S can be obtained separated from the pump-probe contributions described in Eq. 2.1. Two different datasets will be measured, one with phase $\phi_{34} = \Delta\phi$ and a second with $\phi_{34} = \Delta\phi + \pi$. The pump-probe contributions give rise to a constant offset in the data, while the signal of interest $E_1^*E_2E_3E_4^*$ changes sign upon phase inversion. Subtraction of the two datasets gives the intended signal (Fig.2.4). The need of introducing the initial phase of $\Delta\phi$ in the experiments will be explained in chapter5.

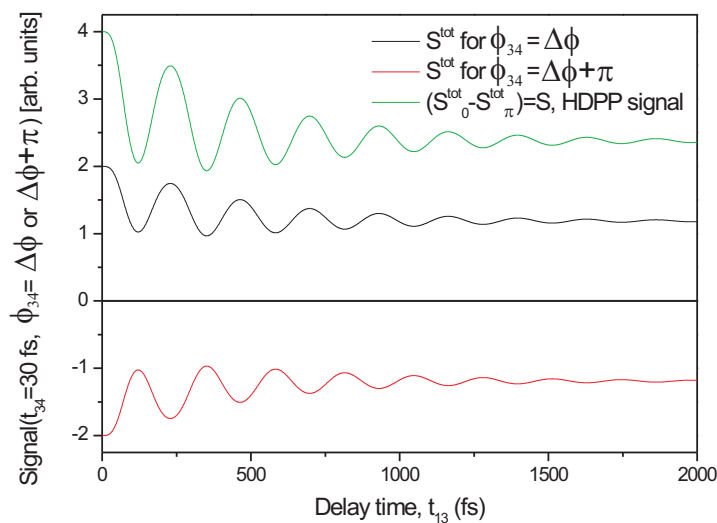


Figure 2.4: Simulations of HDPP experiments showing two datasets with a π phase shift between them. After subtraction the HDPP signal is obtained.

Both the time and the phase control can be acquired using a liquid crystal spatial light modulator (SLM). This device can shape pulses by reprogrammable computer controlled masking. The phase

ϕ_{34} can be controlled electronically while in classical experiments it was controlled in a mechanical way. Electronic control is more stable than mechanic methods that suffer from external fluctuations. A femtosecond Ti:sapphire will be build to provide the ultrashort input pulses. The beam that comes from the laser will be split into two, one part will form the excitation pulse, the other will enter the pulse shaper creating the probe pulse and the heterodyne pulse in the form of a pulse pair (Fig.2.3).

Chapter 3

Titanium Sapphire Laser

In the early 1990's there was a breakthrough in spectroscopy when the self-mode-locked femtosecond Ti:sapphire laser was developed [8]. This allowed the study of dynamics of microscopic systems with an ultrafast time resolution. Since it came into use the self-mode-locking Ti:sapphire laser was for example used in nonlinear optical experiments. In the experiments the laser will be used to generate femtosecond input pulses for the pulse shaping set-up. The key principles and the outline of the Ti:sapphire laser will be discussed in this chapter.

3.1 Pulse generation

A resonator cavity of a laser is usually designed to provide optimal support for only one spatial mode (TEM00), however it supports more than one longitudinal mode. In a Ti:sapphire laser this number can be as high as 10^6 . To obtain pulses, there must be some phase relation between these modes. When all initial phases are set to zero, short pulses are obtained. When mode-locking a laser, the competition between the modes is organized to keep the relative phase constant subsequent Fourier transformation gives a periodic pulse train. As governed by the uncertainty principle, an ultrashort pulse in the time domain corresponds to a broad spectrum in the frequency domain. The gain medium should therefore have a broad line width to generate short pulses. The group velocity dispersion (GVD), causes different frequency components of the broad spectrum to make the round trip through the cavity at different speeds. This tends to broaden the pulse. To generate pulses shorter than a picosecond, this effect should be opposed by putting additional material, that introduces GVD of the opposite sign, in the laser. A prism pair compressor could be used as such [9].

3.2 Kerr-lens mode-locking

The anharmonic motion of bound electrons in a solid a Ti:sapphire crystal give rise to the Kerr effect. The nonlinear refraction index, truncated at the second order, can be described according to Eq.3.1.

$$n = n_0 + n_2 I \quad (3.1)$$

Usually the nonlinear contribution n_2 is very small, however the intensity of the Ti:sapphire laser is sufficiently high to make this contribution substantial. This causes an intensity dependent phase modulation that follows the pulse intensity profile. With a positive n_2 , the index of refraction is larger at the center of a Gaussian pulse than at the sides. In this way a Gaussian lens is formed that focuses the beam. This is counter-effected by the linear diffraction, which balances the Kerr effect (Fig. 3.1).

3.3 Stability zones

The resonator cavity is designed to allow amplification of radiation. The length L_{12} should be designed to be n times the wavelength of the fluorescent near infrared light emitted by the Ti:sapphire crystal. This type of laser has two different zones I and II in the resonator length in which stable pulses are

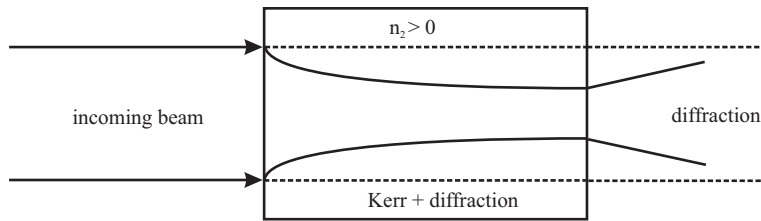


Figure 3.1: Self-focusing of a laser beam in a nonlinear medium with positive n_2 . The diffraction opposes the focusing of the Kerr effect.

produced. The stability zones can be calculated using the ABCD matrix formalism. The parameters of the experimental setup are taken into account. [10]. The formalism describes optical elements (e.g. mirrors) by a 2 by 2 matrix using the assumption that there is little angular displacement of the beams. Multiplication of the matrices of all individual elements, results in the overall matrix of a set-up. This formalism can be adopted in a resonator with the restriction that upon repeating round trips the matrix does not diverge. The representation of the stability zones in figure 3.2 is based on the description of the set-up in section 3.4. The optimal condition for the laser to operate in a high-intensity mode-locked mode is near the low distance border of the second stability zone. In this region, the pulse compressing effects described above create the shortest (approximately 13 fs) and most stable pulses.

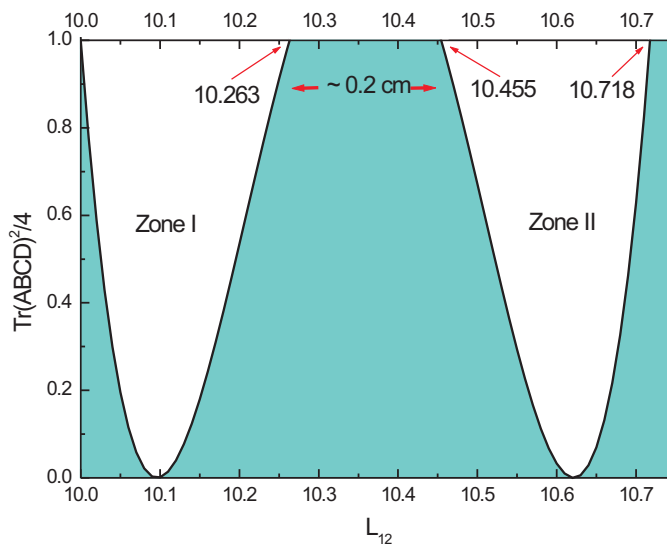


Figure 3.2: Stability zones of the mode-locked laser obtained by applying the ABCD matrix formalism. The initial distance between the two curved mirrors is set at 10 cm.

3.4 Setup

The setup of the laser is outlined in figure 3.3. A Ti:sapphire laser is an optically pumped solid-state laser. The pump is an argon ion laser, which output is focused in the 0.15% doped, Brewster cut Ti:sapphire crystal. The optical cavity is established by two flat mirrors, one high reflector and one output coupler that reflects only a part of the infrared light. After the fold in the reflecting arm there are two possible pathways depending on whether or not prism $P1$, which is mounted on a translation stage, is put into the beam. Without prism $P1$ in the beam, the light is reflected by the high reflector $HR1$ and the laser operates in CW mode. When the prism is positioned just to clip the beam, deflecting it towards prism $P2$ and high reflector $HR2$, the laser can be mode-locked and operates in a pulsed mode. Both arms ($M1$ - $P1$ - $P2$ - $HR2$ and $M1$ - $HR1$) are of equal length to provide identical stability conditions. The resonator cavity is formed by the two curved mirrors $M1$ and $M2$.

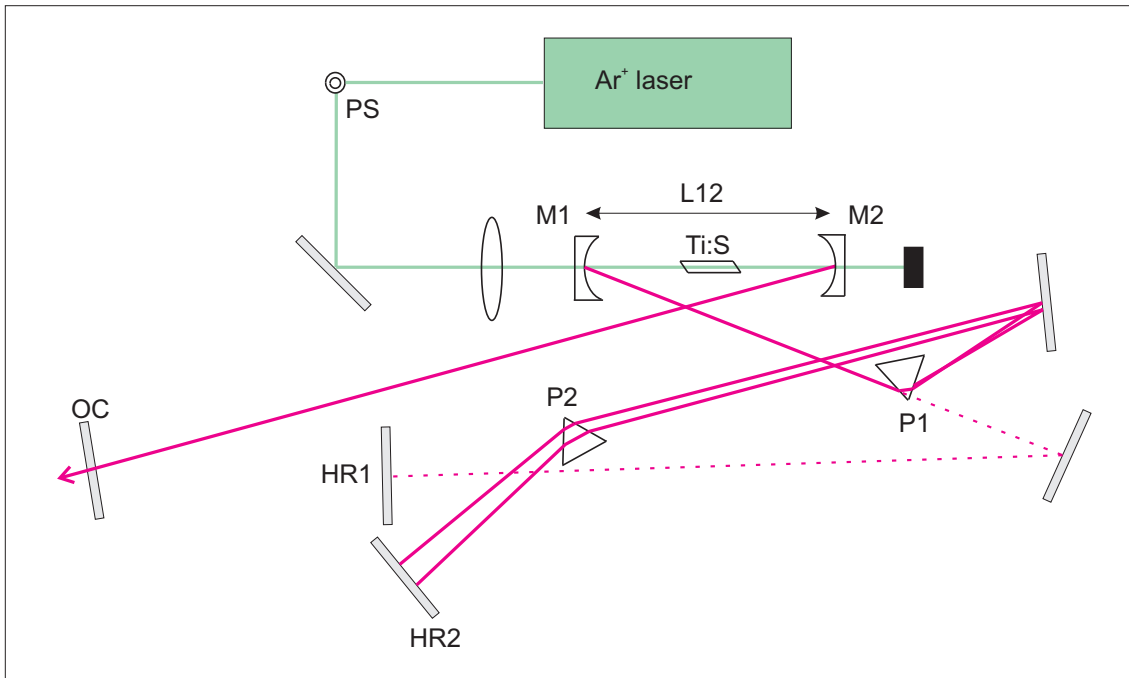


Figure 3.3: Schematic of the mode-locked Ti:sapphire laser. The output of an argon ion laser is focused into a Ti:sapphire crystal. Depending on the position of prism $P1$, the laser will operate in the *CW* or mode-locked mode.

These mirrors are dichroic, reflecting the near infrared light emitted by the Ti:sapphire crystal and transmitting the light of the pump laser. The polarization of the pump beam is rotated by a periscope to be horizontal in order to allow for optimal overlap between pump and resonator modes. To avoid overheating of the crystal, the mount is continuously cooled with tap water. The mode-locked regime is entered by rotating prism $P2$ quickly in or out of the beam.

3.5 Results

To observe the shape and the duration of the pulses from the Ti:sapphire laser, the laser pulse was split into two identical parts by a beam splitter. The translation stage in one of the arms of the set-up delayed one pulse with respect to the other by a time τ . The two beams were focused in the nonlinear BBO crystal that generated a second harmonic signal (SHG) when the beams overlapped in space and in time. The intensity autocorrelation in this non-collinear geometry was obtained background free and is described by Eq.3.2.

$$I^{SHG}(t, \tau) = \int_{-\infty}^{\infty} |E(t) + E(t - \tau)|^2 dt \quad (3.2)$$

The intensity autocorrelation $I(\tau)$ trace had an experimental full width half maximum (FWHM) $\Delta\tau$. By choosing a realistic pulse shape for the pulses that were produced by the Ti:sapphire laser the FWHM Δt of the pulse was retrieved. The assumption that the pulses from the laser had a Gaussian shape led to the factor $\Delta\tau/\Delta t = 1.41$ (for $sech^2$ shape this factor is 1.54) [11]. Figure 3.4 shows a typical example of the autocorrelation trace that was obtained from the Ti:sapphire laser and the accompanying laser spectrum obtained via detection with an OMA system.

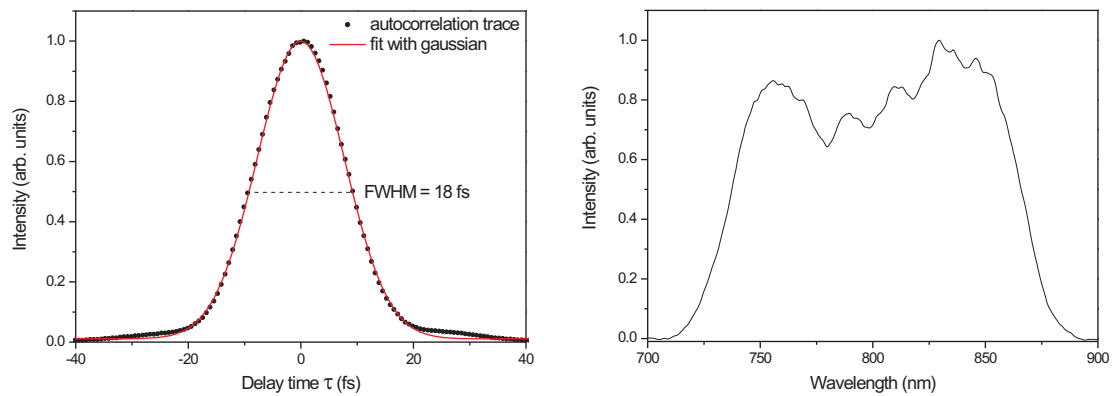


Figure 3.4: Autocorrelation trace of the laser pulses that was obtained in nonlinear geometry via SHG and the accompanying spectrum. The FWHM of the autocorrelation was 18 fs, which corresponded to a pulse duration of 12 fs.

Chapter 4

Spatial Light Modulator (SLM)

The relaxation dynamics after photoexcitation in many systems have components that occur on sub-picosecond timescales [12], [4], [13]. The Ti:sapphire laser has become the workhorse of laser spectroscopy and routinely produces 10-20 fs pulses. The generation of ultrashort pulses is well-established, however the characterization and phase control remain non-trivial [11]. With the development of optical pulse shapers in the early nineties a reliable and easy tool was established to make ultrashort pulses according to specific needs (Fig.4.1) [14]. Extremely complex pulse shapes as in figure 4.1 can be created straightforwardly. A two-dimensional SLM is used to steer the incident pulse to different positions in space and in time.

Many successful pulse shaping techniques rely on masking of the spatially dispersed frequency spectrum. One of the most interesting and well developed methods uses a spatial light modulator (SLM). The SLM is based on a reprogrammable optical mask and this specific design will be discussed below [15], [16], [17]. The pulse shaper will be used to shape a pulse pair. The pulse pair will be used in the pulse sequence for HDPP experiments. The SLM allows full control over the phase and the time delay between the pulses (Fig.4.2).

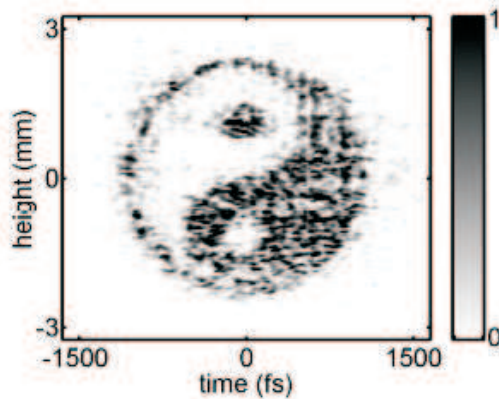


Figure 4.1: Cross-correlation of a waveform generated by pulse shaping. The phase pattern needed on the SLM to generate this shape is iteratively calculated by the Gerchberg-Saxton algorithm [14]

4.1 Pulse Shaping

All pulse shaping techniques are based on the principle of time-invariant filtering. The filter, characterized by its frequency response function, leads to an output signal that is the product of the input signal and the response function. The basic set-up in all shaping experiments have a common layout, based on a pulse compressor. The first diffraction grating (Fig.4.1) spatially disperses the frequency components of the incoming beam that needs to be parallel to the optical table for convenient alignment.

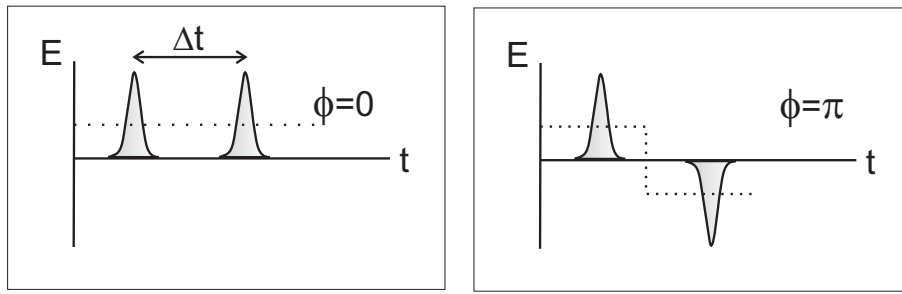


Figure 4.2: Electric field of a pulse-pair created by the SLM. Between the pulses the phase can be changed by π . This causes a change in sign of the electric field. The time t_{34} can be set according to preferences.

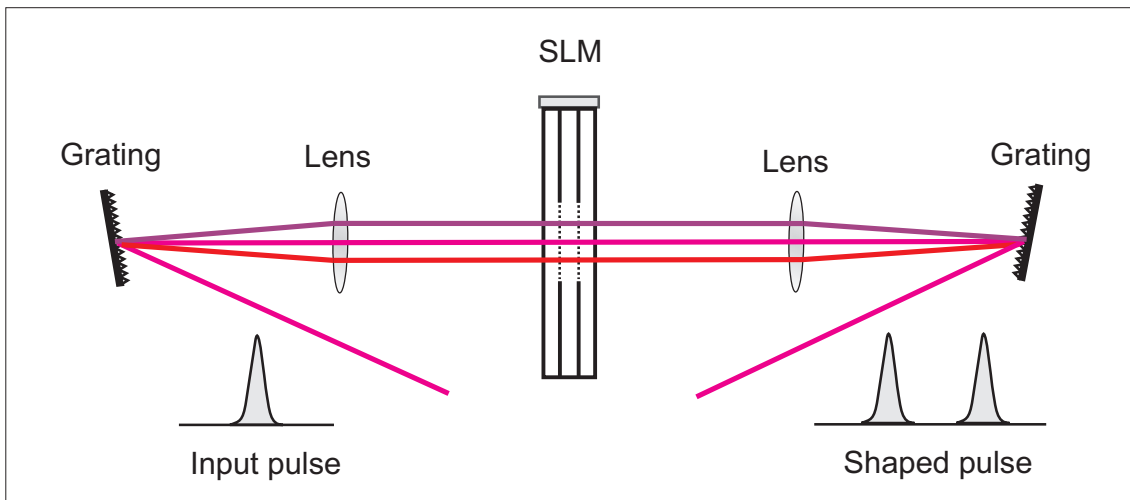


Figure 4.3: Basic outline of a programmable pulse shaper in $4f$ geometry. The grating spatially disperses the beam, after which the lens focuses it in the SLM plane. The second lens-grating pair reverses the action of the first to form a homogenous spot.

The first lens is positioned at the focal distance from the first grating, focusing the dispersed beam in the vertical direction. The spatial light modulator is placed at the center of this focus in the back focal plane of the first lens. The second lens and grating are placed in the same geometry as the first couple at the opposite side of the SLM. Without modulations the output beam should equal the input, to assure that the lenses are used as a one-to-one telescope. For pulses as short as 10-20 fs extra care must be taken with chromatic aberration of the lenses. This problem can be circumvented by using spherical mirrors, however they must be positioned in such a geometry to avoid astigmatism [18].

The most widely used pulse shaper is the computer controlled liquid crystal spatial light modulator (LC SLM). The basic apparatus has one array of nematic liquid crystal held between two glass plates. The crystal consists of long, thin, rod-like molecules that change their orientation upon the application of an electric field. The glass plates also act as a substrate for a transparent ITO (indium tin oxide) layer, that is patterned forming 127 electrodes for 127 separate pixels. Application of an electric field in the horizontal direction (Fig 4.4) changes the orientation of the molecules from the vertical direction to an orientation along the electric field [19].

The tilt of the molecules is proportional to the amplitude of the applied voltage. The rotation of the molecules towards the horizontal axis changes the refractive index for vertically polarized light. With the use of one array and a polarizer the amplitude of the light can be controlled, however this also causes a phase change. Therefore two arrays are required to allow independent change of both the amplitude and phase of the incoming pulses.

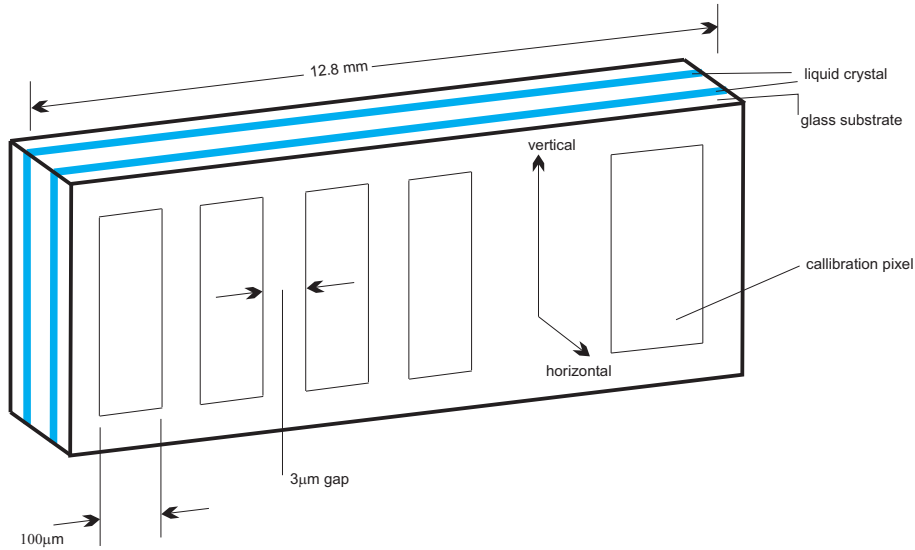


Figure 4.4: Schematic view of a computer controlled LC SLM with phase and amplitude modulation. The 127 pixels have a width of $100 \mu\text{m}$ and are separated by $3 \mu\text{m}$ gaps.

4.2 Liquid crystal spatial light modulator (SLM)

The SLM-256 CRI consists of two liquid crystal arrays through which the light travels consecutively. Both elements contain 127 pixels that can be individually addressed with 4096 different driver levels. The optical axes of the two LC arrays are crossed, so the slow axis of the first array is perpendicular to the fast axis of the second. The presence of two optical elements provides a way to modulate both the amplitude (a supplementary polarizer is needed to transform the polarization rotation to an amplitude modulation) and the phase of passing light pulses according to Eq.4.1 and Eq.4.2.

$$T = \cos^2\left(\frac{\pi[R1 - R2]}{\lambda}\right) \quad (4.1)$$

$$\phi = \frac{\pi(R1 + R2)}{\lambda} \quad (4.2)$$

Both the transmittance, T , and the phase, ϕ depend on the retardance, R . Application of an electric field to the liquid crystal changes the orientation of the molecules. The pathlength of the light that travels through the liquid crystal arrays depend on the orientation of the molecules. By changing the electric field, the light is retarded.

4.3 Set-up: shaper and detection geometry

The design of the pulse shaper is changed with respect to the original version (Fig.4.1). The lenses cause problems with formation of reproducible pulses. It is advisory to stay near the optical axis of a lens because of possible chromatic aberration, however the spatially separated frequencies filled the lens completely. This is likely to cause deviations from a plane wavefront, after which the second grating is unable to invert the frequency spread to one homogeneous spot. To avoid the use of lenses and reduce the number of variables, the set-up was folded by placing a back-reflecting mirror directly behind the SLM (Fig.4.5).

The output beam from the laser is split into two. One part will enter the pulse shaper while the other part is used to cross-correlate the shaped beam in a nonlinear BBO crystal. Temporal overlap of the beams is regulated by a translation stage. The pulse duration is obtained from the FWHM of the second harmonic signal (Fig.3.4).

The top view of the improved shaper shows the set-up in which the lenses are replaced by a spherical mirror ($R=250 \text{ mm}$) (Fig.4.6). By changing the height of the beam on this mirror as shown

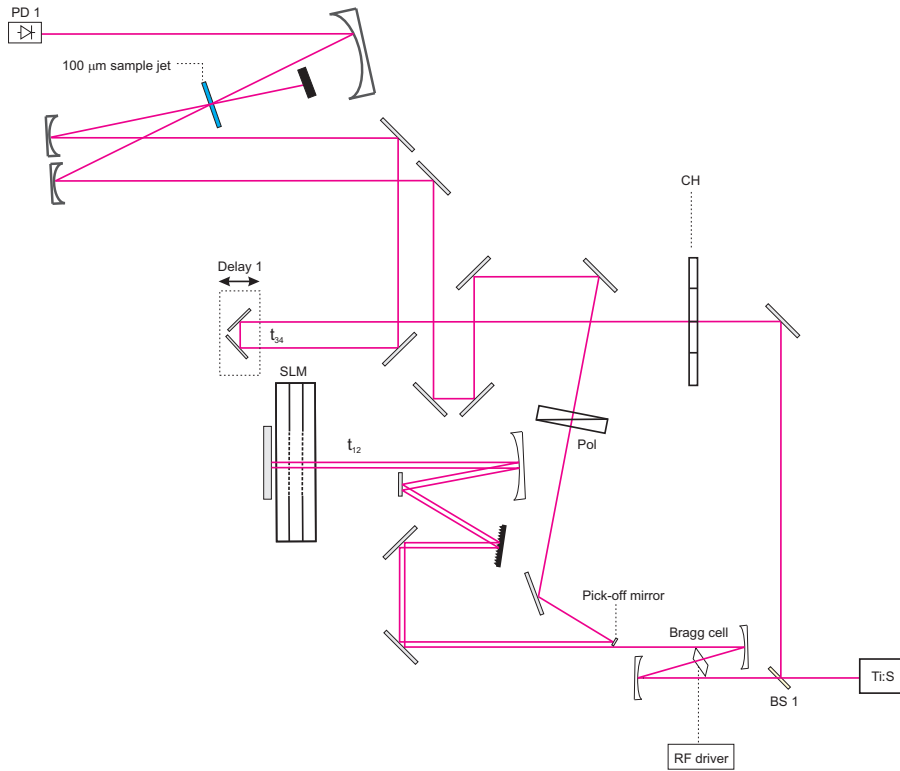


Figure 4.5: Schematics of the pulse shaping set-up. The output of the laser is split into two, the first beam is sent into the pulse shaper, while the second beam acts as a gate to cross-correlate the shaped beam. In the testing phase the sample jet is replaced by a nonlinear BBO crystal.

in the side view (Fig.4.6), the back-reflection geometry can be used. The light is reflected back to a lower spot on the spherical mirror by the flat mirror behind the SLM. The outgoing (shaped) beam travels below the incoming beam creating a possibility to separate the two by a low standing mirror. This mirror does not block the incoming beam and reflects the outgoing beam to the interferometer. The amount of optics and variables are reduced while a double pass through the SLM is obtained. The double pass can be used for higher modulation. The spots of the incoming and outgoing beam on the spherical mirror, the grating and the other mirrors should lie in the same plane perpendicular to the optical table to prevent that incoming and reflected beam travel through different pixels of the SLM. The height difference between the two beams needs to be as small as possible to prevent large effects from spherical aberration.

4.4 Alignment and calibration

Alignment of the shaper geometry and calibration of the SLM are crucial to obtain the desired and expected output waveforms. The following procedure results in optimal alignment of the shaper, when the incoming beam is parallel to the optical table. Firstly, the grating is placed in this beam with its rulings perpendicular to the table. With this setting zero and higher orders of diffraction lie in the same plane parallel to the table. The mirror, on a micrometer, is positioned one focal length away from the grating (250 mm). Secondly, the position of the back-reflecting mirror is in the back focal plane of the mirror. The distance between the two mirrors can be adjusted to obtain a one-to-one telescope, however in practice it does not work optimally. The angle of the back-reflecting mirror puts the spot of the reflected beam right underneath the spot of the incoming beam on the grating. The SLM is positioned directly before the back reflecting mirror. Finally the distance between the grating and the elliptical mirror is adjusted to reach the shortest pulse duration (by looking at the correlation via an external BBO crystal).

Calibration of the SLM is essential to shape pulses in an accurate and reproducible way. First the wavelength calibration is performed to connect the specific pixels to the wavelength of the light that is

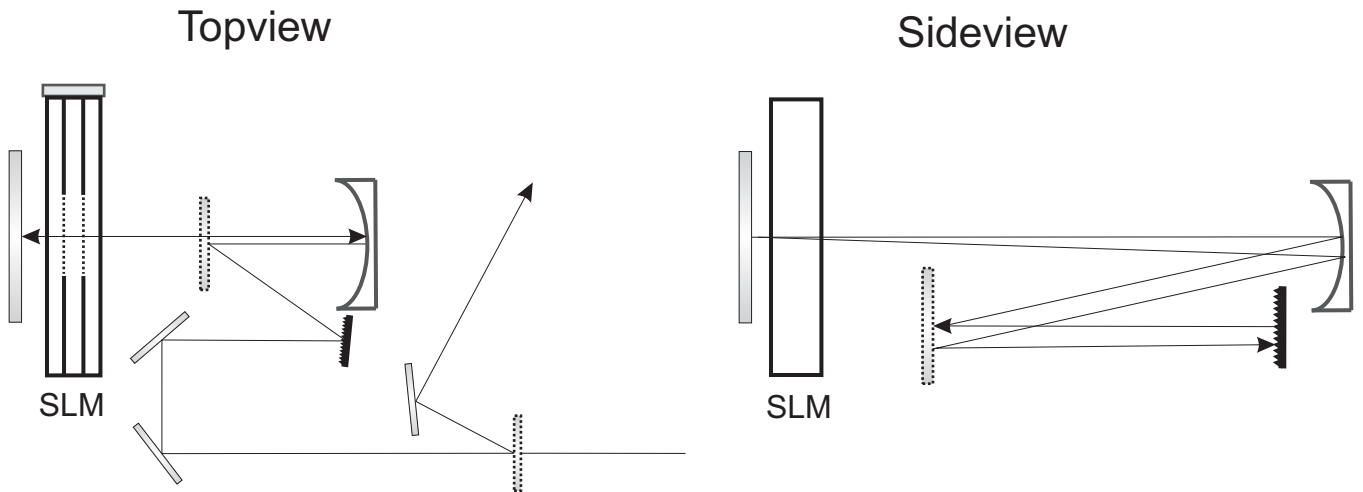


Figure 4.6: Top- and sideview of the pulse shaper, showing the geometry of the incoming and outgoing beams.

passing through it. All pixels are ‘closed’, blocking the light, after which every tenth pixel is ‘opened’ and the light that is passing through is detected with an OMA system. Subsequently the retardation of the light for a specific voltage is obtained. This is done by measuring the transmission at a specific pixel for all 4096 driver settings. In accordance to Eq.4.1 a cosine behavior is obtained (Fig.4.7-A). There is no uniform period of oscillation in this curve, while the orientation of the liquid crystals is not likely to change linearly with the applied electric field. The curve does not change when measured at different pixels, only one pixel is used in the calibration to keep it a fast procedure. The curve in figure 4.7 is fitted and the parameters from this fit give the retardance versus the driver settings (Fig.4.7). The procedure is performed twice, because there are two arrays. In Fig.4.7 the results for only one of the arrays is presented, the curve of the second array looks similar.

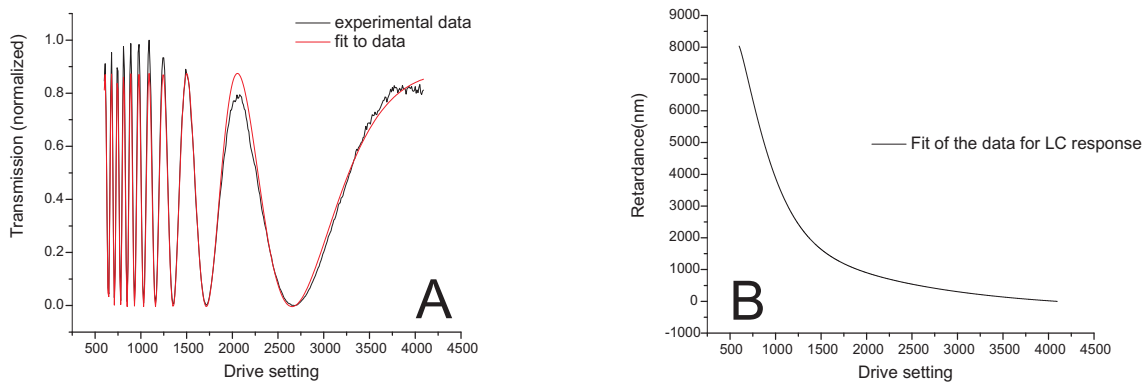


Figure 4.7: A] Transmission of a single array versus the drive settings of the SLM. B] The retardance versus the drive settings obtained from fitting parameters of A. The curves are shown for a single array, because the calibration of the second array looks similar.

The accuracy of this calibration method is tested in a very simple way. The calibration is successful if there is no light detected by the OMA system when all pixels are closed.

4.5 Creation of a pulse pair

To create and control the two pulses necessary for performing HDPP experiments inverse Fourier transformation is used to determine the modulation needed to on the SLM (Fig.4.8). The pulse pair can be described by a sum of two Gaussians (Eq.4.3). Fourier transformation of the pulse shape results in the corresponding spectrum (Fig.4.8). Application of a phase shift of π in the second pulse of the

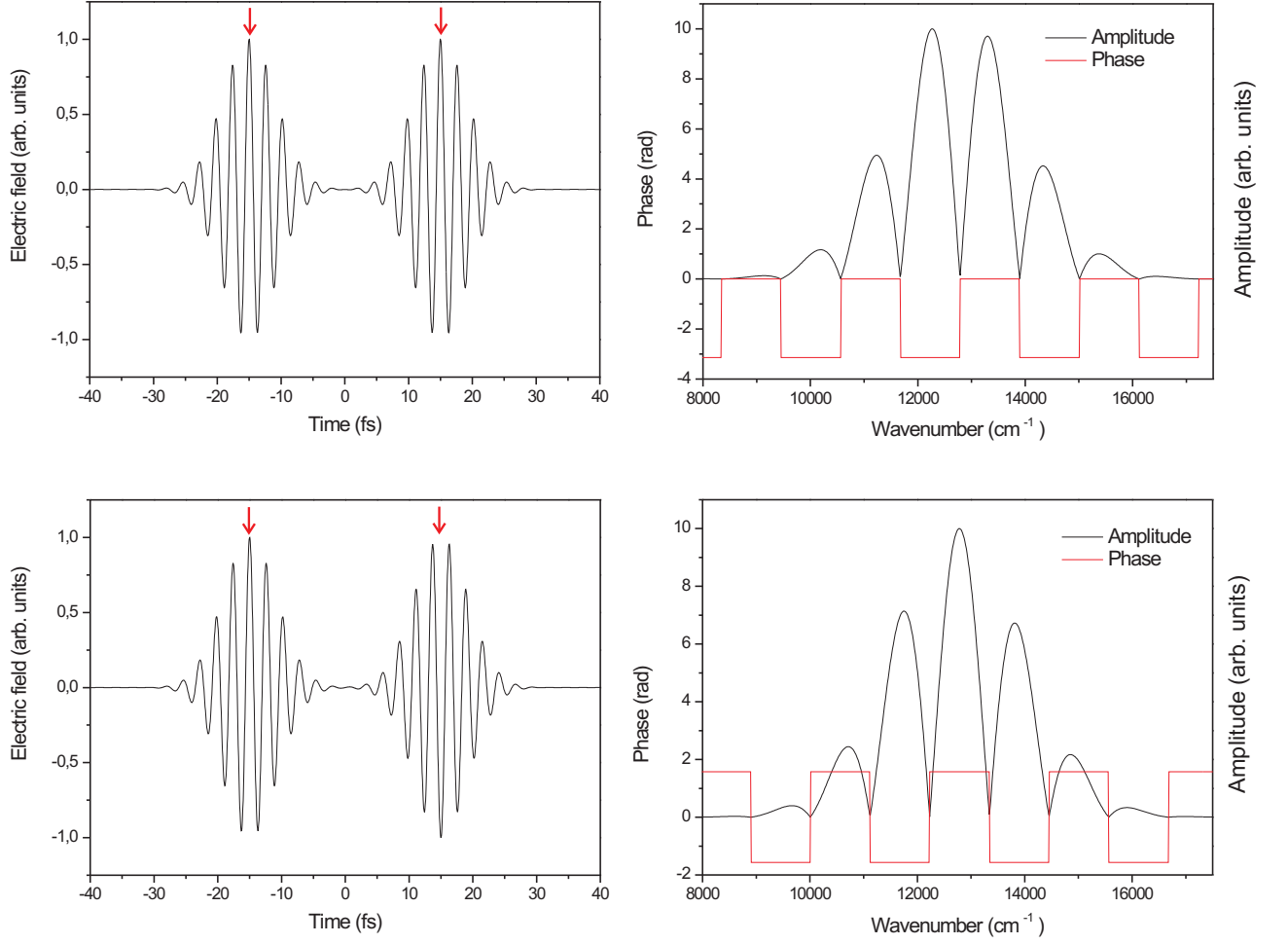


Figure 4.8: Amplitude of a pulse pair as described in Eq.4.3 and its corresponding spectra obtained by Fourier transformation. The arrows point out the π phase shift between the two pulses in the pulse pair in the top and the bottom figures.

pulse pair results in a shift in the Fourier transformed spectrum that can be observed directly.

$$E(t) \propto \sin(\omega(t - t_0) + \phi) \exp^{-(t-t_0)^2/\Delta t^2} + \sin(\omega(t + t_0) + \phi) \exp^{-(t+t_0)/\Delta t^2} \quad (4.3)$$

It appears that the spectrum can be obtained by applying a sinusoidal function to the input field of the laser. A pattern needs to be created on the SLM according to Eq.4.4.

$$T = 1 - \sin^2[\pi \times PHz \times t_{34} + \Delta\phi] \quad (4.4)$$

$$\phi = 0 \quad \text{if } \cos[\pi \times PHz \times t_{34} + \Delta\phi] < 0$$

$$\phi = \pi \quad \text{if } \cos[\pi \times PHz \times t_{34} + \Delta\phi] > 0$$

The initial phase $\Delta\phi$ is used to optimize the modulation depth in the HDPP signal as will be described in chapter 5. The number of PHz represents the frequency of the light that travels through the pixel at that moment. The product of $\pi \times PHz \times t_{34}$ is referred to as the modulation frequency F . From Eq.4.3 it can be derived that the period of the fringes in the spectrum P is directly related to the time between the pulses t_{34} (Eq.4.5). The two pulses are centered at the time t_0 .

$$t_0 = \frac{1}{Pc}$$

$$t_{34} = 2t_0$$

$$t_{34} = \frac{2}{Pc} \quad (4.5)$$

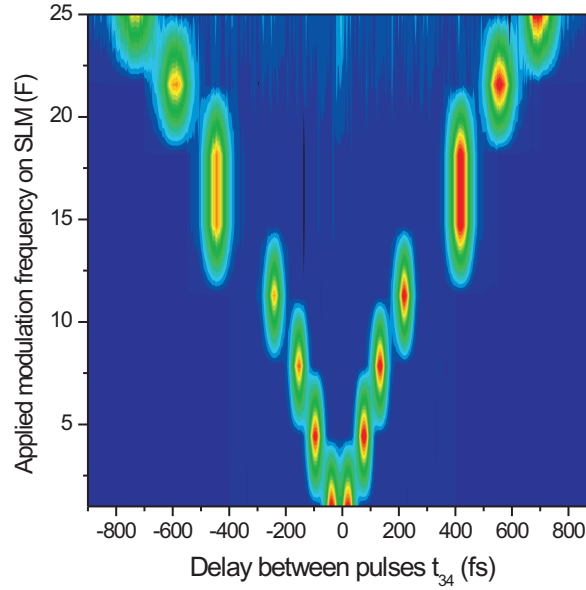


Figure 4.9: Cross-correlations of pulse pairs created by a sinusoidal mask on the LC SLM (Eq.4.4). The time between the pulses t_{34} is linear with the applied frequency. A decrease in the oscillation period leads to increasing of t_{34} (Eq.4.5).

The time separation between the pulses t_{34} can be increased by decreasing the oscillation period, hence by increasing the modulation frequency F .

4.6 Results

The figure shows that by increasing the applied modulation frequency F (y-axis) the delay time t_{34} can be increased (x-axis). The Gaussian intensity profile of the pulses is represented by the different colors in the graph. The time difference between the pulses, t_{34} could be controlled up to about 1 ps. As observed the intensity of the two cross-correlated pulses was not equal, this was not caused by a slightly asymmetric laser spectrum. Simple calculations showed that even with an asymmetric spectrum, the sinusoidal modulation in Eq.4.4 and a subsequent Fourier transformation give pulses of equal intensity. The cause of this deviation is not clear, however in the HDPP experiments a product of the electric fields of the two pulses was used. As a consequence, the deviation will not have had a negative effect on the measurements. The intensity of the pulse pair decreased with the applied frequency, as was also noticed during tests with a He-Ne laser. A high modulation frequency caused the SLM to act as a phase grating spreading around several tens of diffraction orders.

Chapter 5

Acquirement of the Correlation Function

All requirements for HDPP experiments are met. As described in the previous chapter, the two delay times t_{13} , t_{34} and the phase ϕ_{34} can be controlled (Fig.4.9).

5.1 Initial settings

The femtosecond excitation, probe, and heterodyne pulses in the experiments were generated by a home-built Ti:sapphire laser of which the set-up is described in section 3. The full repetition rate (82 MHz) was used for the experiments at an output power of approximately 300 mW. The energy of the pulses at the sample jet was 30 mW, which corresponds to pulse energies in the order of 4 nJ. Accumulation effects can not be excluded with this high repetition rate. The system has not decayed entirely to its ground state when the next excitation pulse arrives. These effects manifest itself by either positive or negative offsets at negative time delays t_{13} . The excitation pulse was focused in the sample jet of 100 μm thickness, after passing a delay stage to control the delay time t_{13} . The pulse duration at the sample position was 20 fs as was deduced from SHG cross-correlation measurements using a 100 μm thick BBO crystal, assuming a Gaussian pulse shape. The concentration of the solution was kept low to prevent first order processes ($P^{(1)}$) to contribute to the signal. The intensity of the pulses also needed to be kept low, to prevent interference of the fifth order processes ($P^{(5)}$). The stimulated signal S^{tot} was detected on the background of the probe pulse (which is inherent to pump-probe spectroscopy), in the phase matching condition $\vec{k}_s = \vec{k}_1 - \vec{k}_1 + \vec{k}_2$. The total signal was detected with a photodiode and processed with a lock-in amplifier.

HDPP experiments were performed on solute-solvent systems. The choice of solute was based on the fact that data was needed for comparison with the measurements. The dye molecule DTTCI is a logical choice while it has already been studied extensively by photon-echo spectroscopy [7]. Furthermore, both the absorption and the emission bands of this dye are covered by the spectrum of the Ti:sapphire laser (fig.5.1). The pump and probe overlap with both the absorption and the emission band of the dye. Solutions of DTTCI (3,3'-diethylthiatricarbocyanine iodide, Aldrich 99%, Fig.5.1) were prepared in the solvents ethylene glycol (ACROS, 99%) and acetonitrile (ACCROS, 99%) by sonication. Absorption measurements were carried out using a standard spectrometer (Perkin Elmer Lambda 900). The optical density of both solutions was kept below 0.4 at the centre of the absorption spectrum.

The theoretical signal described in Eq.2.11 was used to fit the data, the parameters can be found in table 5.1 and were obtained from previous studies [7]. Note that the solvent dynamics in acetonitrile are faster than in ethylene glycol. The correlation time of system bath fluctuations $1/\Lambda$ is shorter in acetonitrile than in ethylene glycol according to these numbers. Because acetonitrile molecules can more easily adapt to changes in the DTTCI configuration.

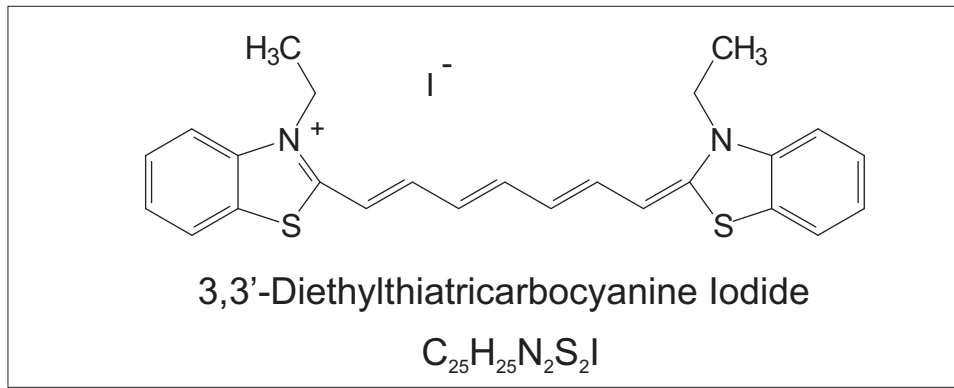


Figure 5.1: Chemical structure of 3,3'-Diethylthiatricarbocyanine Iodide (DTTCI).

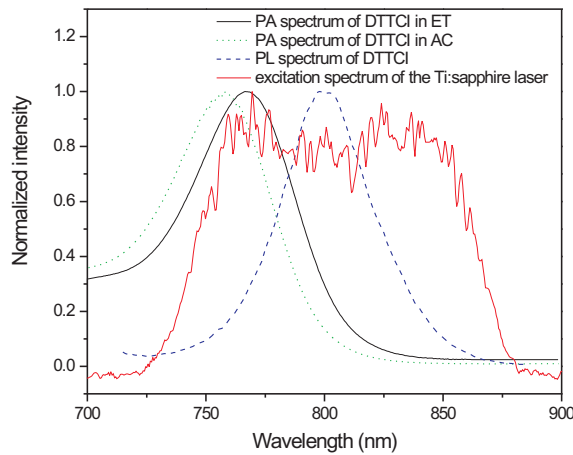


Figure 5.2: The photonabsorption (PA) and photoemission (PE) bands of the dye molecule DTTCI show considerable overlap with the laser excitation spectrum. The absorption of DTTCI in acetonitrile is blue shifted by 10 nm due to destabilization of the excited state of the dye molecule by the solvent.

5.2 Experiments

The experiments were started by positioning the sample jet at the crossing of the pump and probe beam. The pump-probe signal was optimized at $t_{34}=0$, and $t_{13} \approx 1$ ps to ensure the first pulse came before the third pulse. The pump-probe signal had not decreased much by this time delay.

Experimental parameters could be changed to obtain a large HDPP signal and logically an optimal value for the correlation function M that was obtained from this. Equation 2.11 showed that in the HDPP experiments there were two parameters that could be changed, the delay time t_{34} and the phase ϕ_{34} .

At a delay time $t_{13}=220$ fs the phase ϕ_{34} is changed from 0 to 2π at different times t_{34} . The value of 220 fs is chosen, because this is the position of the maximum of the wavepacket oscillations (chapter 2) [7]. The amplitude of the oscillations in the HDPP signal has a maximum when the difference between $S_{\Delta\phi}^{tot}$ and $S_{\Delta\phi+\pi}$ (modulation depth) is maximum. Figure 5.3 shows that the modulation depth decreases with t_{34} . The decrease is due to the exponential term in Eq.2.11. Further, the maximum modulation depth occurs for every t_{34} at different values of $\Delta\phi$.

On the other hand, the time t_{34} in the oscillating part of Eq.2.11 acts a multiplication factor in front of the correlation function. The delay time should be as large as possible for a maximum value of the correlation function.

As a compromise between the two arguments for the choice of t_{34} this value is set at 30 fs in the heterodyne detected pump-probe experiments. At the start of every measurement the optimal position of $\Delta\phi$ was determined by scanning the phase ϕ_{34} from 0 to 2π at the delay times $t_{13}=fs$ and

| Ethylene glycol | Acetonitrile |
|--------------------------|--------------------------|
| $\Delta_w = 0.03[PHz]$ | $\Delta_w = 0.03PHz$ |
| $\omega_w = 0.028[PHz]$ | $\omega_w = 0.028[PHz]$ |
| $\gamma_w = 0.006[PHz]$ | $\gamma_w = 0.008[PHz]$ |
| $\Delta_o = 0.03[PHz]$ | $\Delta_o = 0.03[PHz]$ |
| $\Lambda_o = 0.001[PHz]$ | $\Lambda_o = 0.003[PHz]$ |

Table 5.1: Parameters of the Brownian oscillator used in simulations for solutions of DTTCI in ethylene glycol and acetonitrile. The subscripts w and o denote the weakly and the overdamped case respectively.

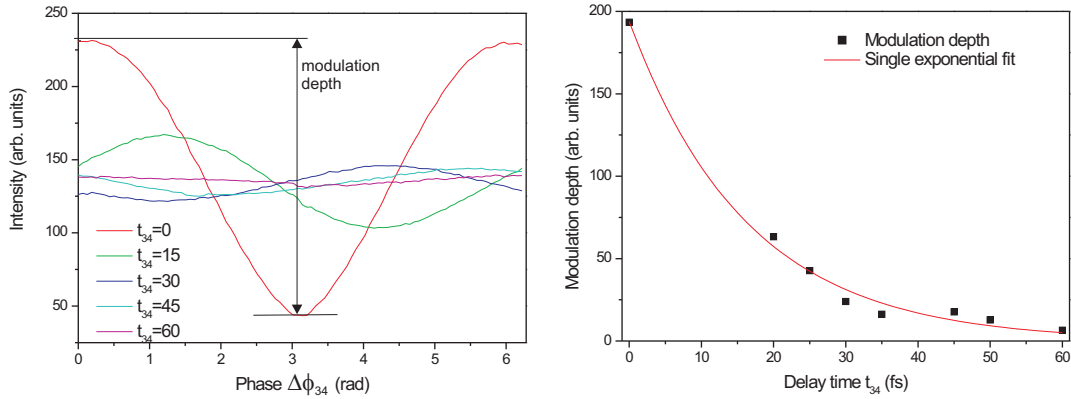


Figure 5.3: Modulation depth of the pump-induced probe signal while the phase $\Delta\phi_{34}$ runs from 0 to 2π . The signal decreases exponentially with increasing time delay t_{34} , vanishing at 60 fs.

$t_{34}=30$ fs. The time t_{13} was scanned to obtain the time evolution of the induced signal S^{tot} .

5.3 Results

Figure 5.4 shows the dynamics of DTTCI in ethylene glycol. The oscillations represent the vibrational motion of the wavepacket dynamics. It must be noted that the original data of S^{tot} showed an offset in the experimental curves at $t_{13} < 0$. This was a result of the high repetition rate of the laser (82 MHz). Upon arrival of the second pulse sequence, the effect of the previous excitation was not completely gone. This meant that in 10 ns the system had not relaxed back to its ground state completely. These offsets were removed from the data by shifting the baseline to a value where S_{tot} for $t_{13} < 0$ was equal to zero.

The HDPP data were fitted nicely with the theoretical signal S derived in section 2 Eq.2.11. To fit the two observed signals $S^{tot}(\Delta\phi)$ and $S^{tot}(\Delta\phi+\pi)$, the equation for S (Eq.2.11) was supplemented with the pump-probe contributions $E_1^*E_2E_3E_3^*$ and $E_1^*E_2E_4E_4^*$. This was achieved for both pump-probe contribution by setting $t_{34}=0$ in the equation for S .

The measurements were repeated in acetonitrile (Fig.5.5), and were fitted with the equations derived from theory. It was clearly visible that the oscillations of the wavepacket dynamics were damped faster than in ethylene glycol as was observed from table 5.1. The stability of the sample jet of acetonitrile was inferior to the one created by ethylene glycol, hence the signal to noise ratio was lower in acetonitrile solutions compared to ethylene glycol solutions.

The oscillations in the HDPP signal were damped faster in acetonitrile than in ethylene glycol. The damping term γ is the inverse population lifetime of the excited state. The values for γ that were obtained from the fits were 0.006 and 0.008 PHz, this agreed with the values that were described in previous studies [7]. The acetonitrile molecules could adapt faster to the conformational changes in the DTTCI molecules.

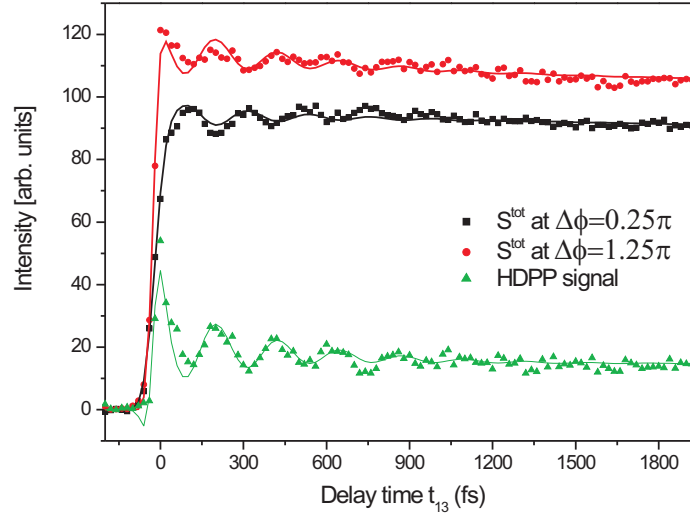


Figure 5.4: Dynamics of DTTCI in ethylene glycol, measured for the settings, $t_{34} = 30\text{fs}$, $\Delta\phi_{34}$ (solid squares), and $t_{34} = 30\text{fs}$, $\Delta\phi_{34} + \pi$ (solid circles). The HDPP signal is obtained by subtracting the signals $S^{tot}(\Delta\phi)$ and $S^{tot}(\Delta\phi + \pi)$ (solid triangles). The simulations (lines), based on the MBO model, agreed with the measurements.

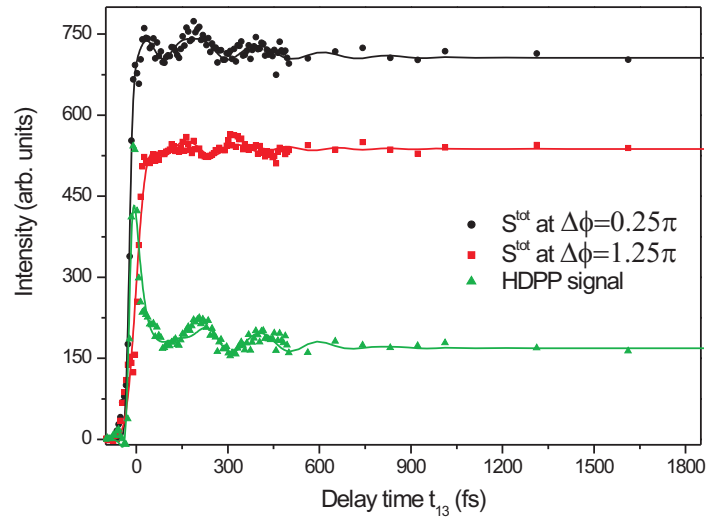


Figure 5.5: Dynamics of DTTCI in acetonitrile, measured for the settings, $t_{34} = 30\text{fs}$, $\Delta\phi_{34}$ (solid squares) and $t_{34} = 30\text{fs}$, $\Delta\phi_{34} + \pi$ (solid circles). The HDPP signal is obtained by subtracting the signals $S^{tot}(\Delta\phi)$ and $S^{tot}(\Delta\phi + \pi)$ (solid triangles). The simulations (solid lines), based on the MBO model, showed that the oscillations were damped on a shorter timescale than in ethylene glycol.

Chapter 6

Conclusion

The goal of this master project was to develop a method to access the solute-solvent correlation function $M(t)$ directly. It is known from classical three-pulse photon echo spectroscopy that this function can be obtained. However, of the parameters that define the coupling between the solute and the bath molecules λ and Δ only the last one is acquired directly. The value of λ is connected with the value of Δ and in this way only the upper limit of λ can be determined. The requirements to be able to obtain λ in a direct way come forward from the theoretical description of photon echo spectroscopy (chapter 2). It turns out that a three pulse sequence, ergo heterodyned pump-probe spectroscopy suffices (Fig.2.3), while in classical photon echo spectroscopy, a four pulse sequence is used. There are three experimental parameters that can be changed t_{13} , t_{34} and ϕ_{34} . The first delay time is regulated mechanically by a delay stage moved by a stepper motor. Most importantly the second delay time t_{34} and the phase ϕ_{34} are controlled electronically by a reprogrammable liquid crystal spatial light modulator.

A spatial light modulator (SLM) can be used as a tool to shape femtosecond optical pulses to specific needs. The advantage of this device over other pulse shapers is that the liquid crystal material inside the SLM is addressed electronically and reprogrammable. This adds to its enormous versatility. The liquid crystal material inside the SLM is divided into 127 separate pixels that change their orientation according to an applied electric field. The frequency components of incoming pulses are spatially dispersed after which they travel through the SLM. The individual pixels can change both the phase and amplitude of the frequency components creating a pattern. With the use of a sinusoidal pattern (section 4) a pulse pair can be formed with adjustable t_{34} and $\Delta\phi_{34}$.

The beams were spatially dispersed by a grating, after which a spherical mirror was used for focustion in the plane of the SLM. To avoid astigmatism, the angle between the mirror and the SLM was set at zero. A backreflecting mirror was placed behind the SLM to send the shaped beam back slightly lower than its incoming counterpart by making a small angle in the horizontal plane (Fig.4.5 and 4.6). In this configuration the shaped beam could be selected by a low-standing pick-off mirror. The output of the SLM was monitored by frequency doubling in a nonlinear BBO crystal to form a cross-correlated signal with the first pulse. This set-up gave reproducible pulse shapes and pulse durations (down to 10 fs FWHM).

Heterodyned photon echo experiments were carried out with the following settings: $t_{12} = 0$, $t_{34} = 30$ fs, $\Delta\phi_{34}$ and $t_{12} = 0$, $t_{34} = 30$ fs, $\Delta\phi_{34} + \pi$. The total signal S^{tot} consists of three contributions. Two pump-probe contributions $E_1^*E_2E_3E_3^*$, $E_1^*E_2E_4E_4^*$ and the HDPP contribution $E_1^*E_2E_3E_4^*$ (Eq.2.1). Only the last term is related to the correlation function. Changing the phase between the third and the fourth pulse by π and measuring the time-evolution of S^{tot} for both cases, resulted only in a change of sign of the HDPP contribution. Subtraction of the two datasets resulted in pure HDPP signal S . To be able to compare the data obtained by heterodyned pump-probe measurements, a test sample was chosen that had already been studied by photon echo spectroscopy [7].

Solutions of the dye molecule DTTCI in both ethylene glycol and acetonitrile were used in the experiments. The HDPP signal obtained from experiments on these solutions showed definite signs of the correlation function. Next to the fact the data were fit nicely with the theoretically deduced signals

for S^{tot} and S (section 2), a second sign of the correlation function was observed. The oscillations of the wavepacket that originated from the excitation of a vibrational manifold (section 2) inverted upon a phase change by π . Pump-probe measurements do not depend on the phase and could therefore not have caused this phenomena.

In conclusion, the set-up including the SLM was very suitable to generate pulse pairs that can be time and phase controlled. The measurements showed a trend that could clearly not be explained solely by pump-probe contributions and were a direct indication that the solvent-solute correlation function $M(t)$ was obtained.

A disadvantage of the current system was the fact that the pump-induced signal was detected on the background of the probe pulses (3 and 4). The intensity of these pulses saturated the detector, hence an optical density filter had to be introduced. This unfortunately also reduced the intensity of the induced signal by the same amount.

Now this simple system appears to work well, the technique can be adapted to 2D photon echo experiments. The phase matching conditions of this experiments result in the appearance of the signal in a background free direction (boxcar geometry). This photon echo technique will be used to study coherent transport in arrays of oriented chromophores on nanowires.

Chapter 7

Appendix

Using the Feynman formalism, it is possible to calculate the final signal of the four-wave mixing experiments. There are four resonant Feynman diagrams for heterodyne detected pump probe experiments (Fig.7.1).

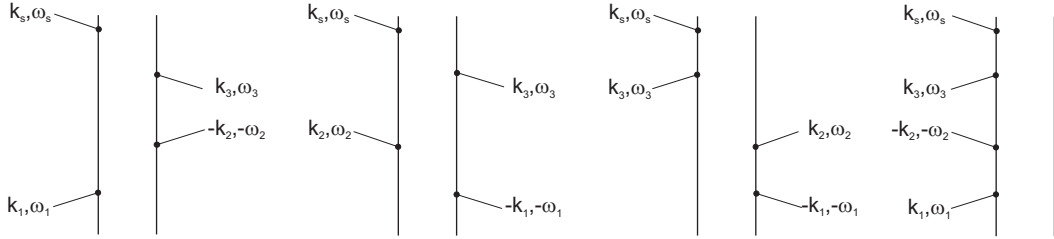


Figure 7.1: Interactions with the corresponding electric fields.

The four diagrams contribute equally in the Liouville equation which then eventually leads to Equation 7.1.

$$\begin{aligned}
 P^{(3)}(t, t_{13}) = & \left(\frac{i}{\hbar}\right)^3 \int_{\infty}^0 dt_1 dt_2 dt_3 \vec{\mu}_{ab}^2 \vec{\mu}_{ba}^2 e^{-i(\omega_b - i\gamma_{ba})(t_1 + t_3)} e^{-\gamma_{bb}t_2} e^{-i\omega(t-t_3)} e^{i\omega(t-t_3-t_2)} e^{-i\omega(t-t_3-t_2-t_1)} \times \\
 & E_3(t-t_3) E_2^*(t-t_3-t_2) E_1(t-t_3-t_2-t_1) + \\
 & \left(\frac{i}{\hbar}\right)^3 \int_{\infty}^0 dt_1 dt_2 dt_3 \vec{\mu}_{ab}^2 \vec{\mu}_{ba}^2 e^{-i\omega_b(t_3-t_1) - \gamma_{ba}(t_3+t_1)} e^{-\gamma_{bb}t_2} e^{-i\omega(t-t_3)} e^{i\omega(t-t_3-t_2)} e^{-i\omega(t-t_3-t_2-t_1)} \times \\
 & E_3(t-t_3) E_2(t-t_3-t_2) E_1^*(t-t_3-t_2-t_1) + \\
 & \left(\frac{i}{\hbar}\right)^3 \int_{\infty}^0 dt_1 dt_2 dt_3 \vec{\mu}_{ab}^2 \vec{\mu}_{ba}^2 e^{-i\omega_b(t_3-t_1) - \gamma_{ba}(t_3+t_1)} e^{-\gamma_{aa}t_2} e^{-i\omega(t-t_3)} e^{i\omega(t-t_3-t_2)} e^{-i\omega(t-t_3-t_2-t_1)} \times \\
 & E_3(t-t_3) E_2(t-t_3-t_2) E_1^*(t-t_3-t_2-t_1) + \\
 & \left(\frac{i}{\hbar}\right)^3 \int_{\infty}^0 dt_1 dt_2 dt_3 \vec{\mu}_{ab}^2 \vec{\mu}_{ba}^2 e^{-i(\omega_b - i\gamma_{ba})(t_1 + t_3)} e^{-\gamma_{aa}t_2} e^{-i\omega(t-t_3)} e^{i\omega(t-t_3-t_2)} e^{-i\omega(t-t_3-t_2-t_1)} \times \\
 & E_3(t-t_3) E_2^*(t-t_3-t_2) E_1(t-t_3-t_2-t_1)
 \end{aligned} \tag{7.1}$$

This formalism assumes homogenous frequency broadening (Lorentzian lineshape) and is a simplification of the description in the two-level system. However, changing the dephasing parameter γ into the response functions $R(t_3, t_2, t_1)$ effectively will lead to equation 2.11.

Bibliography

- [1] R. Boyd. *Nonlinear optics* (Academic Press, Amsterdam, 2003).
- [2] S. Mukamel. *Principles of nonlinear optical spectroscopy* (Oxford University press, New York, 1995).
- [3] S. Yeremenko. *Water Dynamics Explored by Femtosecond Infrared Spectroscopy* (PrintPartner-Ipskamp, Enschede, 2004).
- [4] T. Joo, Y. Jia, J.-Y. Yu, D. M. Jonas, and G. R. Fleming. *Dynamics in isolated bacterial light harvesting antenna (lh2) of Rhodobacter sphaeroides at room temperature*. *Journal of Physical Chemistry* **100**, 2399 (1996).
- [5] P. D. F. G. Y. M. I. N. Prall, B.S. *Two-dimensional optical spectroscopy: Two-color photon echoes of electronically coupled phtalocyanine dimers*. *Journal of Chemical Physics* **120**, 2537 (2004).
- [6] V. L. V. G. R. Van Amerongen, H. *Photosynthetic excitons* (World Scientific, Singapore, 2000).
- [7] W. De Boeij. *Ultrafast solvation dynamics explored by nonlinear optical spectroscopy* (RUG, Groningen, 1997).
- [8] D. E. Spence, P. N. Kean, and W. Sibbett. *60-fs pulse generation from a self-mode-locked titanium sapphire laser*. *Optics letters* **16**, 42 (1991).
- [9] C. Rullière and et al. *Femtosecond laser pulses* (Springer-Verlag, Berlin, 1998).
- [10] O. Svelto. *Principles of lasers* (Plenum Press, New York, 1989).
- [11] R. Trebino and et.al. *Frequency-resolved optical gating: The measurement of ultrashort laser pulses* (Kluwer academic publishers, Dordrecht, 2000).
- [12] S. Woutersen and H. Bakker. *Resonant intermolecular transfer of vibrational energy in liquid water*. *Science* **402**, 507 (1999).
- [13] B. Kraabel, D. McBranch, N. S. Sariciftci, D. Moses, and A. J. Heeger. *Ultrafast spectroscopic studies of photoinduced electron transfer from semiconducting polymers to c60*. *Physical Review B* **50**, 18543 (1994).
- [14] J. C. Vaughan, T. Feurer, and K. A. Nelson. *Automated spatiotemporal diffraction of ultrashort laser pulses*. *Optics Letters* **28**, 2408 (2003).
- [15] M. M. Wefers and K. A. Nelson. *Generation of high-fidelity programmable ultrafast optical waveforms*. *Optics letters* **20**, 1047 (1995).
- [16] T. Feurer, J. C. Vaughan, R. M. Koehl, and K. A. Nelson. *Multidimensional control of femtosecond pulses by use of a programmable liquid-crystal matrix*. *Optics letters* **27**, 652 (2002).
- [17] T. Hornung, J. C. Vaughan, T. Feurer, and K. A. Nelson. *Degenerate four-wave mixing spectroscopy based on two-dimensional femtosecond pulse shaping*. *Optics letters* **29**, 2052 (2004).

- [18] A. M. Weiner. *Femtosecond pulse shaping using spatial light modulators*. Review of scientific instruments **71**, 1929 (2000).
- [19] D. Demus and et. al. *Handbook of liquid crystals; fundamentals* (Wiley-VCH, New York, 1998).

Acknowledgements

I would like to thank the following persons for contributing to my research project:

- Maxim, for giving me the opportunity to work on this project and for his daily supervision
- Ben, for helping me out with all the technical problems in the lab
- Foppe, for solving every computer problem one can possibly think of and for developing the programs needed for the experiments
- Dan, for answering all questions and for letting me raid your lab in search of mirrors
- Dimiter, for joining and helping me with the project (good luck with your future experiments)
- All the other group members